Geophysical Research Letters®

Key Points:

- Elevated temperature promotes a more uniform fluid pressure distribution over the fault surface mainly by reducing water viscosity
- Accelerated and enhanced fault healing at elevated temperature causes faster fault slip rates upon injection-induced fault failure
- The injection-induced seismic hazard is enhanced in higher-temperature geothermal reservoirs and deeper part of the reservoirs

Transition From Slow to Fast Injection-Induced Slip of an Experimental Fault in Granite Promoted by Elevated Temperature

Yinlin Ji[1] , **Hannes Hofmann[1,2]** , **Ernest H. Rutter[3]** , and **Arno Zang[1]**

[1]Helmholtz Centre Potsdam GFZ German Research Centre for Geosciences, Potsdam, Germany, [2]Institute of Applied Geosciences, Technische Universität Berlin, Berlin, Germany, [3]Rock Deformation Laboratory, Department of Earth and Environmental Sciences, The University of Manchester, Manchester, UK

Abstract The influence of elevated temperature on injection-induced fault slip is poorly constrained. In this study, at steady-state elevated temperatures, triaxial shear-flow experiments on a sawcut fault in granite were conducted to simulate injection-induced slip of a critically stressed fault. Our results suggest that an elevated temperature favors a more uniform fluid pressure distribution over the fault surface mainly by reducing water viscosity. At temperatures above ambient, a larger perturbation force from the injected fluid is required to reactivate the fault primarily because of the enhanced thermally activated fault healing processes, resulting in a faster fault slip rate upon failure. This study may partially explain the causal link between higher reservoir temperature and higher maximum magnitude of injection-induced earthquakes in geothermal systems, and the observation that larger magnitude seismic events concentrate near the deeper part of the reservoir, where temperature is higher.

Plain Language Summary It is imperative to explore the poorly constrained influence of elevated temperature on injection-induced fault slip to explore the implications for injection-induced seismicity in geothermal reservoirs. To this end, we injected water with a similar temperature to the host rock into a laboratory-scale fault in granite under a critically stressed condition at constant elevated temperatures to simulate injection-induced fault slip beyond the limited cooling zone near the injection well in geothermal reservoirs. The reduced water viscosity promotes a more uniform fluid pressure distribution on the fault surface at elevated temperature. The perturbation force upon fault reactivation provided by the injected fluid increases with higher temperature, indicating an accelerated and enhanced fault healing at higher temperature. Fault friction reduces under the stress relaxation experimental condition, while fault healing can partially compensate for the friction reduction associated with relaxation. The fault strength recovery at elevated temperature may have caused the faster fault slip rate upon failure. The higher injection-induced seismic hazard associated with higher geothermal reservoir temperature, and the concentration of larger magnitude events near the deeper part of the Basel geothermal reservoir could be partially explained by the findings of this study.

1. Introduction

Climate change and the associated extreme weather events have made it necessary to achieve carbon neutrality. As an alternative to fossil fuels, almost carbon-free geothermal energy can potentially make a significant contribution to energy supply by producing heat from the earth. By far the largest amount of geothermal energy is stored in low-permeability formations. Large-scale worldwide utilization of geothermal energy therefore depends on the effective stimulation of tight geothermal reservoirs. Hydraulic stimulation is currently an indispensable technique for reservoir permeability enhancement by creating new fractures (i.e., hydro-fracturing) and/or inducing the shear slip of fractures/faults (i.e., hydro-shearing), forming an enhanced geothermal system (EGS) (Ellsworth, 2013; Olasolo et al., 2016; Schoenball et al., 2020). Although most injection-induced seismic events are micro-seismic events, some large magnitude earthquakes have been reported, leading to the termination of EGSs, like the Pohang (Grigoli et al., 2018; Kim et al., 2018) and Basel (Mukuhira et al., 2016) projects. Therefore, there is an urgent need to advance our understanding of injection-induced seismicity in geothermal systems.

Injection-induced seismic events, especially larger magnitude ones, are primarily generated by shearing of fractures/faults caused by fluid injection (Ellsworth, 2013). Fluid injection elevates the pore pressure and reduces the effective normal stress on a shear-oriented fault, potentially causing fault reactivation and seismicity (e.g.,

Ji & Wu, 2020; McGarr, 2014; Wang et al., 2020). Other indirect processes associated with fluid injection may also induce/trigger seismic events, including the stress changes due to thermo-poroelasticity (e.g., Chang & Segall, 2016; De Simone et al., 2017; Deng et al., 2016; Segall & Lu, 2015) and earthquake interactions (e.g., Catalli et al., 2013, 2016; Schoenball & Ellsworth, 2017), as well as stress transfer induced by aseismic slip (e.g., Cappa et al., 2018; Cappa et al., 2019). Nevertheless, it is necessary to consider whether the mechanisms of injection-induced seismicity in geothermal systems could be more complex due to the presence of elevated temperature.

In geothermal systems, the temperature contrast between the reservoir rock and the colder injected fluid near the injection well may cause the contraction of the reservoir and unclamp the fault. Both laboratory (KC & Ghazanfari, 2021) and numerical (Huang et al., 2019) studies demonstrate that the cooling-induced contraction of reservoir rock promotes fault reactivation mainly by thermal unclamping. Although cooling-induced fluid contraction and depressurization tend to stabilize the fault by increasing the effective normal stress, it may be compensated by continued fluid injection. Reservoir-scale simulation suggests that whether the thermal stress promotes or prevents the reactivation of the fault depends on the fluid flow direction, the initial stress regime, and the time as well as the location relative to the cooling zone (Jeanne et al., 2017). Apart from the limited cooling zone near the injection well (Im & Avouac, 2021; Jeanne et al., 2017), fractures and faults beyond this zone are subject to fluid pressurization at a steady-state elevated temperature, in which case the injected fluid becomes heated to the reservoir temperature and flows to fractures and faults without causing thermal stress changes. The effect of steady-state elevated temperature on injection-induced fault slip behavior may therefore be of great significance for deciphering injection-induced seismicity in geothermal systems.

Few studies have reported a pronounced effect of steady-state temperature on fault slip behavior. Raising temperature from 200°C up to 400°C has suppressed the occurrence of fast stick-slip events on dry sawcut faults in granite and gabbro (Brace & Byerlee, 1970). In contrast, the transition from creep to slow and fast earthquakes was facilitated by increasing the temperature from 25°C to 100°C on dry sawcut faults in dolostones (carbonates) (Passelègue et al., 2019). These contradictory results may imply that temperature-dependent fault slip behavior is also rock-type dependent. Moreover, injection-induced fault slip at elevated temperature is further complicated by the fluid pressure diffusion process (Ji et al., 2020; Passelègue et al., 2018; Rutter & Hackston, 2017), and thermally activated processes under thermo-hydro-mechanical (THM) conditions (e.g., KC & Ghazanfari, 2021; Blanpied et al., 1995; Rutter & Mainprice, 1978; Tenthorey et al., 2003; Yasuhara et al., 2005). Yet, to date, a systematic investigation of injection-induced fault slip in granite at different steady-state elevated temperature levels is lacking.

Here, we aim to explore experimentally the effect of steady-state elevated temperature (up to 125°C in this study) on injection-induced fault reactivation. We injected water with a similar temperature to the rock matrix into a critically stressed fault in granite and monitored the fluid pressures at the inlet and outlet boreholes, as well as the changes of shear stress and fault slip. This allowed us to identify the temperature effect on injection-induced seismicity by comparing the fault slip rate and friction coefficient upon fault reactivation. We finally provide some inferred implications for injection-induced seismicity in geothermal systems.

2. Materials and Methods

2.1. Materials

The experiments were performed on Odenwald granite, sourced from Rimbach, Germany. The granite contains mainly quartz, feldspar, and mica, with a mean grain size of ~2 mm (Kluge et al., 2020). This macroscopically homogeneous granite is characterized by a porosity of ~0.6%. The permeability of the granite was measured as ~1 × 10^{-18} m^2 at a hydrostatic confining pressure of 2 MPa and is expected to decrease further at higher effective pressures. The uniaxial compressive strength (UCS) of the granite is approximately 120–140 MPa (Blöcher et al., 2019). For this study, the cylindrical sample was 50 mm in diameter and 100 mm in length and contained a sawcut fault inclined 30° to the sample axis (Figure 1a). The sawcut fault was ground using abrasive paper with a particle size of 30.2 μm, and the two ends of the sample were ground flat and parallel within ±0.1 mm. Two small boreholes with a nominal diameter of 1.8 mm were drilled parallel to the sample axis into the fault surface near the short edges of the sample halves to facilitate pore water communication between endcaps and fault surface. In addition, two horizontal boreholes with a diameter of 2 mm were drilled to intersect the two vertical boreholes
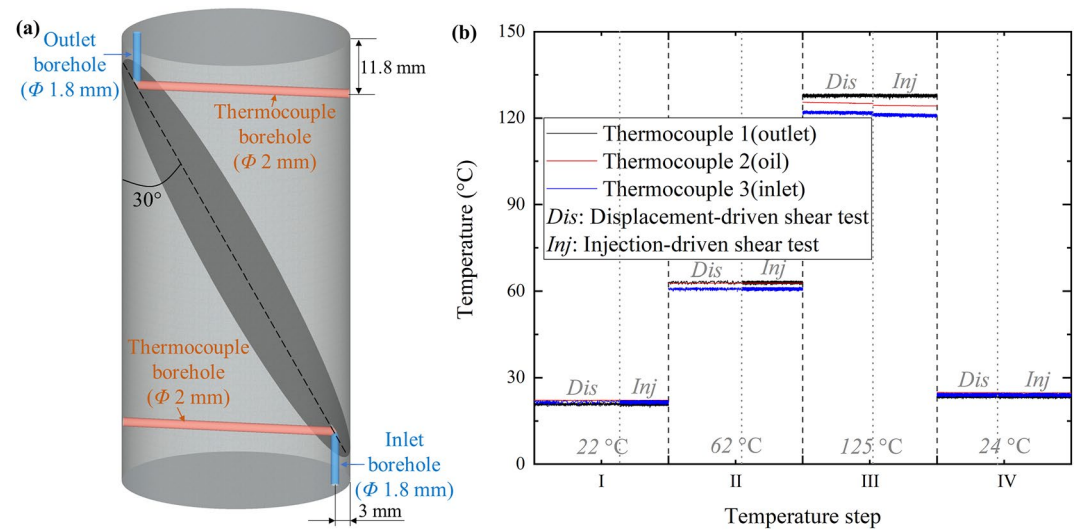
Figure 1. Sample geometry and temperature steps. (a) Schematic drawing of the sample assembly with inlet and outlet boreholes and two horizontal boreholes accommodating thermocouples. (b) Four temperature steps applied in this study. The duration of displacement-driven (dis) and injection-driven (inj) shear tests at each temperature step are normalized by the total experimental time at the respective temperature step.

at the fault surface to accommodate thermocouples for continuous local measurements of fluid temperatures near the inlet and outlet boreholes. The thermocouples fitted tightly into the boreholes, ensuring negligible influence on the dead volume and the fluid flow pathway along the fault. The rock matrix could remain nearly intact during the experiments because of the favorable angle of the sawcut fault in the high-strength and low-permeability granite, and thus the fluid flow was constrained within the fault plane (Ji et al., 2021).

2.2. Methods

In this study, a series of triaxial shear-flow experiments on a sawcut fault in a granite sample was performed using the MTS triaxial deformation apparatus. The sample was first fully saturated at a hydrostatic confining pressure (medium: silicone oil) of 2 MPa and a pore pressure (medium: distilled water) of 0.2 MPa. Then, a sequence of four temperature steps (i.e., 22°C, 62°C, 125°C, and 24°C) were applied to the same sample, starting from room temperature (Figure 1b). Throughout the experiments, one thermocouple was placed inside the confining pressure oil and near the sample to measure the overall sample temperature, and two thermocouples were inserted into the sample to measure the fluid temperatures near the inlet and outlet boreholes (Figure S1 in Supporting Information S1). Two heater bands attached to the triaxial cell and another two cartridge heaters inserted into the baseplate were used to heat the triaxial cell assembly (Figure S2 in Supporting Information S1). We used the full power of the heating system during heating, resulting in a maximum temperature increasing rate of ~0.0086°C/s (~31°C/h). More details on the high-temperature system can be found in Text S1 in Supporting Information S1. The long pore pressure tube passing through the heated baseplate and the confining pressure oil (Figure S1 in Supporting Information S1) ensured that the room-temperature water had been heated to the target temperature before entering the sample. This is supported by the fact that the three thermocouples always showed similar temperature readings with a maximum difference of <6.3% throughout the entire sequence of experiments (Figure 1b), suggesting a steady-state elevated temperature with negligible thermal stress. For each temperature step, when the thermocouple readings reached the target temperature, we waited at least ~2 hr for stabilization before conducting the experiments.

At each temperature step, a displacement-driven shear test was first conducted at a constant axial displacement rate of 1 µm/s to measure the peak shear strength (τ_p) of the fault under 21 MPa constant confining pressure and 1 MPa uniform pore pressure on the fault surface. The shear stress was then lowered to 90% of the peak shear strength by slowly retracting the axial piston. Afterward, the axial piston was fixed, and distilled water was injected via the inlet borehole at 0.2 ml/min while recording the pore pressure near the outlet borehole (constant downstream dead volume during fluid injection). The dead volumes in the up- and down-streams were ~177

and ~67 ml, respectively. The fluid injection was terminated when at least one full slip event was observed. The fixed axial piston during fluid injection imposed a stress relaxation condition (Rutter & Mainprice, 1978). Note that the minimum pore pressure of 1 MPa raised the phase transition (boiling) temperature of pore water to ~180°C, suggesting that pore water remained as liquid throughout all experiments. Thus, in this study, the injection-induced fault slip was simulated at a steady-state elevated temperature beyond the limited cooling region near the injection well in EGSs (Im & Avouac, 2021).

The effective normal stress (σ'_n) and shear stress (τ) on the fault can be calculated from the axial stress (σ_1), confining pressure (σ_3), fracture inclination angle (Ψ) with respect to sample axis and the pore pressure (P) as,

$$\sigma'_n = \frac{1}{2}(\sigma_1 + \sigma_3) - \frac{1}{2}(\sigma_1 - \sigma_3)\cos 2\psi - P = (\sigma_3 - P) + (\sigma_1 - \sigma_3)\sin^2\psi \tag{1}$$

$$\tau = \frac{1}{2}(\sigma_1 - \sigma_3)\sin 2\psi = (\sigma_1 - \sigma_3)\sin\psi\cos\psi \tag{2}$$

The sample shortening (ΔL_s) can be obtained from the total axial displacement (ΔL) monitored by a linear variable displacement transducer (LVDT) installed outside the triaxial cell, the axial force (ΔF) measured by an in-vessel load cell, and the vertical stiffness of the testing system measured as $k_{sys} \approx 796$ kN/mm using,

$$\Delta L_s = \Delta L - \frac{\Delta F}{k_{sys}} \tag{3}$$

The fault slip displacement (ΔL_f) can therefore be estimated as,

$$\Delta L_f = \left(\Delta L_s - \frac{\Delta F L}{EA}\right) / \cos\psi \tag{4}$$

where E is the Young's modulus of the granite, and L and A are the length and cross-sectional area of the cylindrical sample, respectively. The stress, deformation, and hydraulic data were recorded at 10 Hz throughout the experiments. The sample shortening rate and fault slip rate were estimated as the derivatives of sample shortening and fault slip displacement with time at an interval of 0.1 s, respectively. The peak rates of dynamic slip events may be underestimated from the data sampled at 10 Hz (cf., McLaskey & Yamashita, 2017; Ohnaka & Shen, 1999; Passelègue et al., 2019; Xu et al., 2018), but our data allow for the comparison of relative magnitudes of peak rates.

After the experiments, we performed finite element modeling (FEM) to recover the temporal evolution of fluid pressure distribution on the fault surface during fluid injection based on the fluid pressures at the inlet (injection) and outlet (monitoring) boreholes (Text S2, Figures S3–S4, and Table S1 in Supporting Information S1).

3. Results

3.1. Mechanical Stability of the Fault

3.1.1. Displacement-Driven Fault Slip

The mechanical results of triaxial shear-flow experiments at the four temperature steps are presented in Figure 2a (Temperature step I: 22°C), 2c (II: 62°C), 2e (III: 125°C), and 2g (IV: 24°C). The sample shortening calculated from eq. 3 is shown in these figures. The experiment at each temperature step contains a displacement-driven shear test and a subsequent injection-driven shear test. In the displacement-driven shear stage, stick-slip instabilities were observed at room temperature 22°C (Figure 2a) and 62°C (Figure 2c). The average static shear stress drop associated with stick-slip events reduces from ~3.2 MPa at 22°C to ~2.3 MPa at 62°C. When the temperature was increased to 125°C (Figure 2e), the fault exhibited stable sliding behavior. Strikingly, the stick-slip instabilities occurred again with an average static shear stress drop of ~2.8 MPa when the temperature was reduced back to 24°C (Figure 2g). This observation suggests that an elevated temperature tends to suppress fast and unstable displacement-driven fault slip, which is consistent with the results on dry sawcut faults in granite and gabbro reported by Brace and Byerlee (1970). The primary mechanisms responsible for such transition may be related to the changing friction rate parameters (Blanpied et al., 1995, 1998; Scholz, 1998) and changing stiffness of the fault and the testing system with different temperatures (Passelègue et al., 2019).
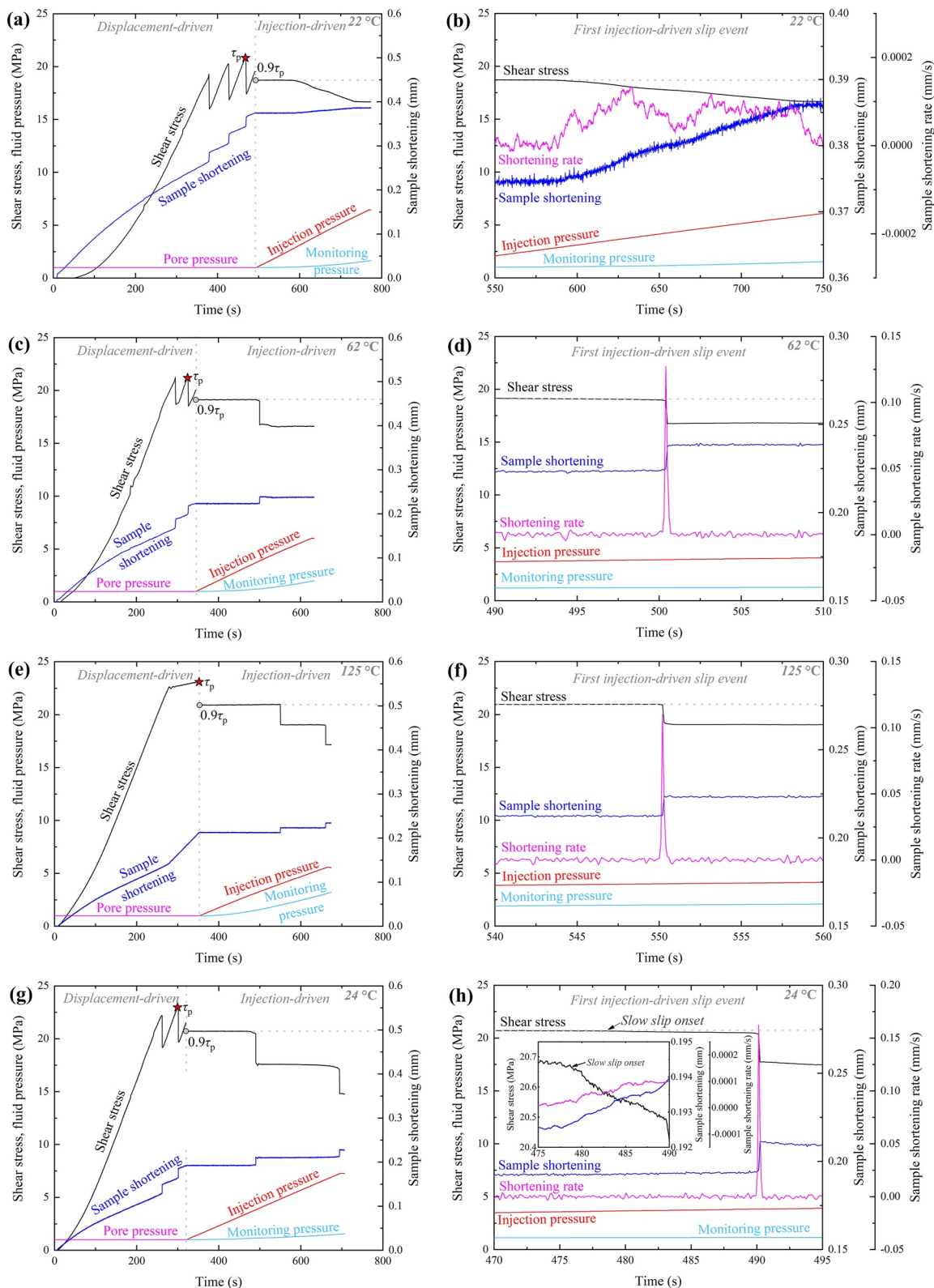
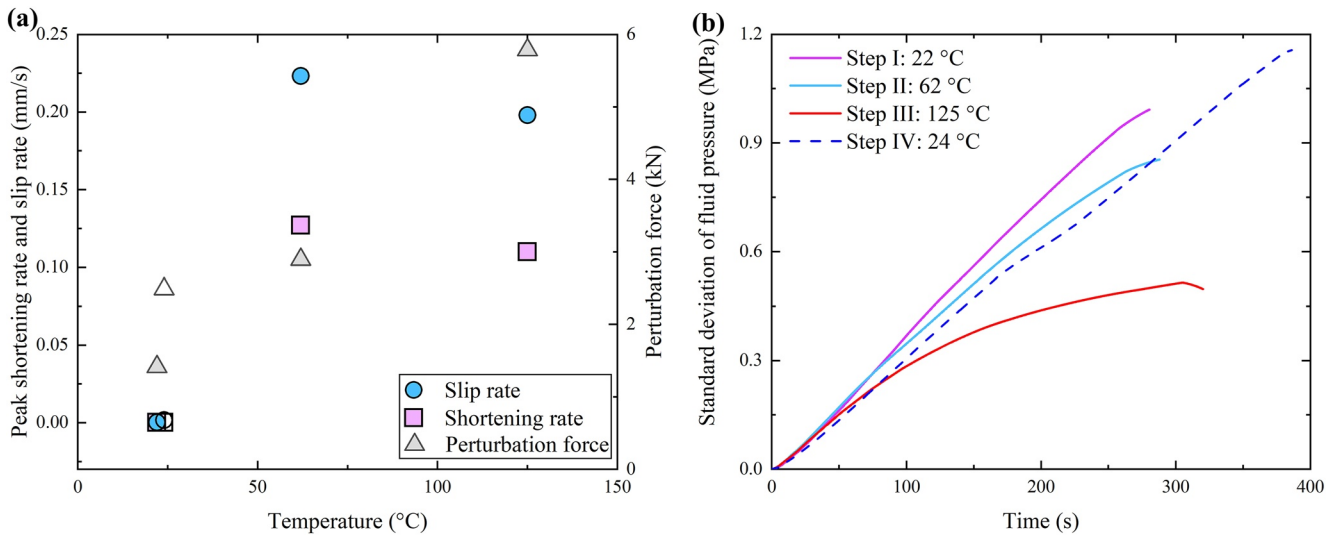**Figure 2.**

3.1.2. Injection-Driven Fault Slip

Following each displacement-driven shear test, the shear stress was adjusted to 90% peak shear strength as measured in the displacement-driven shear test. The subsequent injection-driven shear test was conducted under a stress relaxation condition with the axial piston fixed at each temperature step. Injection-induced stable sliding was observed at room temperature 22°C (Figures 2a and 2b), but the fault showed stick-slip instabilities at higher temperatures of 62°C (Figures 2c and 2d) and 125°C (Figures 2e and 2f) with a static shear stress drop of ∼2.08 and ∼1.94 MPa, respectively. This trend suggests that elevated temperature may promote the transition of injection-induced fault slip from a slow and stable to a fast and unstable character. The injection-induced unstable slip at the final temperature step of 24°C (Figures 2g and 2h) seems not to support the trend suggested by the results from the first three temperature steps. However, unlike in the injection-induced stick-slip events at 62°C and 125°C, the injection-induced stick-slip events at 24°C were preceded by an early-onset and long-lasting slow pre-slip (see inset in Figure 2h). Examination of the fault surface showed that some larger asperities have been damaged, leading to a certain amount of gouge production (see Figure S5 in Supporting Information S1). Thus, we argue here that the injection-induced stick-slip instabilities at 24°C were results of the acceleration of the long pre-slip due to the "lubrication" of gouge (i.e., rolling on wear particles) produced after a large slip displacement of ∼1.1 mm accumulated in the previous test stages (Byerlee, 1967; Reches & Lockner, 2010). A further factor that may have led to this observation is that the effective normal stress upon injection-induced fault slip at the final temperature step of 24°C was ∼1 MPa higher than that at the first temperature step of 22°C, due to the higher resolved normal stress induced by shear hardening, which also favors unstable stick-slip behavior. More details on estimating effective normal stress are presented in Section 4.1. Therefore, slow and stable injection-induced fault slip may still occur at 24°C without gouge-induced fault lubrication and an increased effective normal stress. Taken together, our results demonstrate that elevated temperature tends to promote the occurrence of fast and unstable injection-induced fault slip.

The peak sample shortening rate (eq. 3) and fault slip rate (eq. 4) during the first injection-driven slip events at different temperatures were compared (Figure 3a). Here the fault slip rate was estimated using a constant Young's modulus of granite (E = 64 GPa) measured in a dedicated triaxial compression experiment on Odenwald granite sample with strain gauges, which will cause errors of estimation due to the possible change of Young's modulus during our experiments involving repeated axial loading and unloading. The peak slip rate at the final temperature step at 24°C was the rate just before the pre-slip accelerates to become an unstable stick-slip event. It was found that the peak shortening rate and slip rate both increase with higher temperature, bearing in mind the experimental uncertainties. The perturbation force (see eq. S2 in Text S2 in Supporting Information S1) provided by the injected fluid upon fault reactivation obtained from the numerical model also shows an increasing trend with higher temperature. These results are consistent with the notion that the capability of fault rupture propagation is proportional to the magnitude of local force perturbation (Galis et al., 2015, 2017).

3.2. Fluid Pressure Distribution on the Fault

The delayed increase of the downstream monitoring pressure relative to the inlet injection pressure (Figure 2) suggests a heterogeneous fluid pressure distribution over the fault surface (Ji et al., 2020; Passelègue et al., 2018; Rutter & Hackston, 2017). We use the standard deviation of fluid pressure derived from the numerical model (Text S2 and Figure S4 in Supporting Information S1) to quantify the degree of fluid pressure heterogeneity, which decreases with higher temperature (Figure 3b), indicating that the fluid pressure distribution becomes less heterogeneous as temperature is raised from 22°C to 125°C. As a key parameter controlling the fluid pressure diffusion process, the hydraulic diffusivity D is given as $D = k/\mu s$, where k, μ, and s are permeability, fluid viscosity, and storage capacity, respectively. The water viscosity reduces by ∼4 times from room temperature to 125°C, leading to the increase of time-weighted average hydraulic diffusivity D_a by ∼3 times (see Table S1 in Supporting

Figure 2. Time history of shear stress, fluid pressure (injection and monitoring pressures) as well as sample shortening during the triaxial shear-flow experiments, consisting of a displacement-driven shear test and a subsequent injection-driven shear test, at (a) Temperature step I: 22°C, (c) Temperature step II: 62°C, (e) Temperature step III: 125°C, and (g) Temperature step IV: 24°C. Enlargement of the first injection-induced slip event in each temperature step is shown correspondingly in the right column: (b) Temperature step I: 22°C, (d) Temperature step II: 62°C, (f) Temperature step III: 125°C and (h) Temperature step IV: 24°C. In addition to the parameters shown in the left column, the sample shortening rate is shown in the right-panel figures to illustrate better the slip characteristics. The inset in (h) shows the early-onset and long-lasting slow stable pre-slip before the first injection-induced dynamic slip event at 24°C. Note different scales of sample shortening and sample shortening rate in the right panel. The shortening rate in (b) and the inset in (h), and the sample shortening in the inset in (h) have been smoothed by applying a Savitzky-Golay filter to remove high-frequency noise. τ_p is the peak shear strength denoted by 5-pointed red stars.

Figure 3. (a) Peak shortening rate and slip rate as well as perturbation force upon fault failure as a function of temperature. The open data points show the results at the last temperature step of 24°C. Note that only the results for the first event at each temperature step are shown, because they occur under similar stress conditions. (b) Temporal evolution of the standard deviation of fluid pressure, which quantifies the degree of fluid pressure heterogeneity, during fluid injection at four temperature steps.

Information S1) with some influences from temperature-dependent and slip-dependent fault permeability and storage capacity. The curve for the last temperature step at 24°C is shown as a blue dashed line for reference. The degree of fluid pressure heterogeneity in this case is larger than the case at 125°C but smaller than at 22°C and 62°C, indicating that the fault surface roughness has experienced irreversible changes after the ~1.1 mm cumulative slip displacement in the previous test stages (see Figure S5 in Supporting Information S1). These results suggest that temperature has a primary control on the fluid pressure distribution over the fault surface mainly by changing the fluid viscosity, which may in turn modulate the fault slip behavior.

4. Discussion

4.1. Competition Between Thermally Activated Processes Affecting Fault Friction

The reason why temperature seems to promote the slow-to-fast transition of injection-induced fault slip may be explored by investigating the evolution of the friction coefficient upon approaching failure. In Figure 4a, the shear stress is shown as a function of effective normal stress during the displacement-driven and injection-driven shear tests at each temperature step. The effective normal stress during injection-driven shear tests was estimated by subtracting the average fluid pressure across the fault surface as estimated from the numerical model (Text S2 and Figure S4 in Supporting Information S1) from the normal stress (eq. 1) on the fault. The friction coefficients upon displacement-driven failure and injection-driven failure are generally compatible with Byerlee's rule for rock friction (Byerlee, 1978) generalized from a large amount of displacement-driven shear tests (see gray dash lines in Figure 4a).

The friction coefficient is plotted in Figure 4b as a function of temperature. The displacement-driven peak friction μ_p increases with temperature steps from I (22°C) to III (125°C), primarily caused by the shear hardening associated with cumulative slip displacement (e.g., Ji & Wu, 2020; Noël et al., 2019; Tembe et al., 2010). However, this may also imply that the friction coefficient of granite may be relatively independent of temperature, at least within the temperature range explored in this study, which is consistent with the results reported by Stesky et al. (1974) on sawcut faults in Westerly granite up to 500°C. It is noteworthy that the displacement-driven peak friction μ_p becomes lower at the final temperature step of 24°C, mostly because gouge has been produced after the ~1.1 mm long cumulative fault slip as inferred from the topographic changes of the fault surface (Figure S5 in Supporting Information S1) and thus the fault has been weakened slightly by rolling on wear particles (Byerlee, 1967). Injection-driven reactivation friction μ_r is always lower than the respective displacement-driven peak friction μ_p, but also increases with temperature (Figure 4b). The always-lower injection-driven reactivation
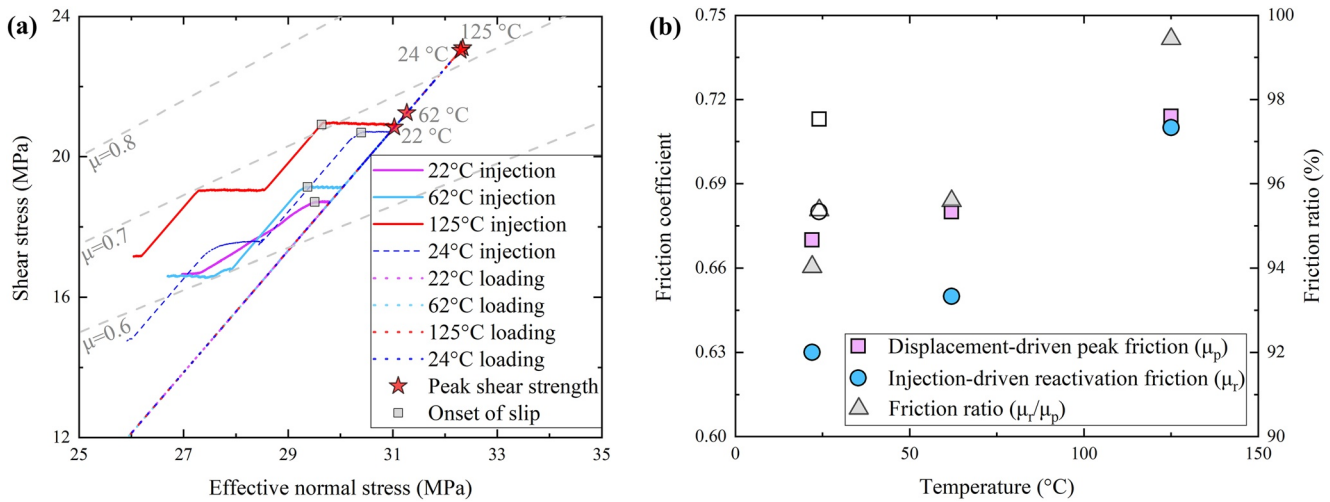
Figure 4. (a) Shear stress as a function of effective normal stress during the displacement-driven shear test and a subsequent injection-driven shear test at the four temperature steps. The four 5-pointed red stars represent the peak shear strengths obtained in the displacement-driven shear tests. The gray squares represent the shear stress upon injection-induced fault reactivation. (b) Friction coefficient and friction ratio of the injection-driven reactivation friction to displacement-driven peak friction as a function of temperature. The open data points show the results at the last temperature step of 24°C.

friction μ_r compared to the displacement-driven peak friction μ_p is consistent with our stress relaxation experimental condition.

The ratio between injection-driven reactivation friction μ_r and displacement-driven peak friction μ_p was calculated, and it increases with higher temperature from 94.0% at 22°C up to 99.4% at 125°C (Figure 4b), indicating a thermally enhanced process has operated which can increase the fault friction in a temperature-dependent and/or time-dependent fashion. Such "fault healing" (e.g., Marone, 1998; Marone et al., 1995; Olsen et al., 1998; Rutter & Maddock, 1992; Tenthorey et al., 2003; Yasuhara et al., 2005) due to temperature-mediated and/or time-mediated processes under thermo-hydro-mechanical conditions can partially compensate for the reduction in fault friction associated with stress relaxation, which is also a thermally activated process but likely characterized by a different Arrhenius rate constant. The ratio μ_r/μ_p is always lower than 100% in our study, indicating that the friction reduction dominates the competition with fault healing under the stress relaxation experimental condition in the hydrothermal environment of the present tests. In addition, the injection time required before the onset of fault reactivation is also longer at higher temperature (Table S1 in Supporting Information S1). That is, enhanced fault healing induced by accelerated thermally activated processes at higher temperature with longer injection time increases the ratio μ_r/μ_p, which in turn tends to increase the perturbation force from the injected fluid required for reactivation and thus increases the fault slip rate upon failure (Im et al., 2017).

Although not specifically explored experimentally in the present study, thermally activated processes causing fault healing are expected to include enhanced dissolution and precipitation of feldspar and quartz in the hydrothermal environment and the resulting cementation-welding of contact area at elevated temperature (KC & Ghazanfari, 2021; Yasuhara et al., 2005), development of adhesion across surfaces through precipitation of minerals that are products of low-grade metamorphic reactions, and diffusive adhesion at asperity tips across surfaces (McLaskey et al., 2012). Thermally activated stress relaxation processes may include pressure-solution slip (Rutter & Mainprice, 1978), sub-critical microcrack growth (Atkinson & Meredith, 1987), and transient or anelastic intracrystalline-plastic creep (Carter & Kirby, 1978). The detailed thermally activated processes operating in injection-induced slip of critically stressed faults at steady-state elevated temperatures merit further studies.

4.2. Implications for Injection-Induced Seismicity in Geothermal Reservoirs

We have here experimentally demonstrated that elevated temperature may promote fast and unstable injection-induced fault slip by accelerating hydrothermal reactions and enhancing fault healing, in the same way that time in the "hold" period of slide-hold-slide tests can do the same thing (e.g., Marone, 1998; Marone et al., 1995). Our experiments provide complementary insights into the mechanisms of injection-induced

seismicity, particularly for the high-temperature effect. Although extrapolation of our experimental findings to higher temperatures and different rock types would be presently too ambitious, these results may partially explain the causal link between higher reservoir temperature and larger maximum magnitude of injection-induced seismic events in various types of geothermal systems with different reservoir rocks, as summarized by Buijze et al. (2019) (Figure S6 in Supporting Information S1).

These results may also provide a plausible explanation for the observation in Basel EGS that larger magnitude post-shut-in seismic events concentrate near the deeper part of reservoir (Figure S7 in Supporting Information S1). Pore pressure migration, as a well-established and accepted mechanism, can only explain why shut-in seismic events appear near the periphery of the seismic cloud (Mukuhira et al., 2016). In terms of the larger magnitude of post-shut-in seismic events near the deeper part, first, it is true that a deeper depth normally means a higher mean pressure and a higher differential stress, requiring a larger pore pressure to reactivate the fault to slip and hence higher local seismic magnitudes. Second, a larger section of the fault may have been induced to slip due to the more uniform pore pressure distribution at the edge of the seismic zone after shut-in (Mukuhira et al., 2016). Third, higher temperatures will raise the pore pressure of injected fluid as they penetrate into the deeper hot zone, leading to thermal pressurization and increase the seismic hazards. In addition to these factors, considering the average temperature gradient of ∼40°C/km at Basel EGS (Ladner & Häring, 2009), the temperature difference can reach ∼40°C between the top (∼3,800 m) and the bottom (∼4,800 m) of the seismic cloud (Figure S7 in Supporting Information S1). Therefore, we may argue from the present experiments that even under otherwise similar conditions, the higher temperature at the deeper part of reservoir could promote the occurrence of faster fault slip and larger seismic events once the pore pressure migrates there after the termination of fluid injection.

Our results are derived from one suite of experiments on a centimeter-scale sawcut fault in granite within a limited temperature range up to 125°C, which may restrict the confident extrapolation of the findings to other rock types and higher temperatures. In future, we see a further necessity to explore temperature effects on injection-induced fault slip with a wider range of parameters on more rock types.

5. Conclusions

We performed a series of triaxial shear-flow experiments on a sawcut fault in granite at four temperature steps (i.e., 22°C, 62°C, 125°C, and 24°C) to simulate injection-induced fault slip at steady-state elevated temperatures. Local temperature measurements showed that there was negligible temperature difference between the injected fluid and the rest of the sample, since the fluid flows through the heated pore pressure tube, suggesting that injection-induced fault slip was stimulated at a region beyond the limited cooling zone of any thermal stress effect near the injection well. The results showed that the fluid pressure distribution across the fault surface becomes more uniform at higher temperatures, primarily due to the reduced water (injection fluid) viscosity. Injection-induced fault slip became faster at higher temperatures, consistent with the increasing perturbation force provided by the injected fluid. A competition developed between thermally activated stress relaxation (friction reduction) and fault healing (friction increase) processes under a stress relaxation condition in the hydrothermal environment. The fault healing partially compensated for the friction reduction under the stress relaxation experimental condition. Elevated temperature was inferred to enhance fault healing and thus to promote a faster slip rate upon eventual injection-induced fault reactivation. These results demonstrate a temperature effect on injection-induced seismicity, which might partly explain: (a) the trend summarized from numerous geothermal sites that the maximum magnitude of injection-induced seismic events increases with higher reservoir temperature, and (b) the observation that larger post-shut-in seismic events concentrate near the deeper part of geothermal reservoir such as in the Basel EGS.

Data Availability Statement

This manuscript is accompanied by Supporting Information. The experimental data presented in this study are available at https://figshare.com/s/96a9e83957c402b3c2e7.

References

Atkinson, B. K., & Meredith, P. G. (1987). The theory of subcritical crack growth with applications to minerals and rocks. *Fracture Mechanics of Rock*, *2*, 111–166. https://doi.org/10.1016/b978-0-12-066266-1.50009-0

KC, B., & Ghazanfari, E. (2021). Geothermal reservoir stimulation through hydro-shearing: An experimental study under conditions close to enhanced geothermal systems. *Geothermics*, *96*, 102200. https://doi.org/10.1016/j.geothermics.2021.102200

Blanpied, M. L., Lockner, D. A., & Byerlee, J. D. (1995). Frictional slip of granite at hydrothermal conditions. *Journal of Geophysical Research: Solid Earth*, *100*(B7), 13045–13064. https://doi.org/10.1029/95JB00862

Blanpied, M. L., Marone, C. J., Lockner, D. A., Byerlee, J. D., & King, D. P. (1998). Quantitative measure of the variation in fault rheology due to fluid-rock interactions. *Journal of Geophysical Research: Solid Earth*, *103*(B5), 9691–9712. https://doi.org/10.1029/98JB00162

Blöcher, G., Kluge, C., Goense, T., Pei, L., Bakker, R., & Bruhn, D. (2019). Hydraulic-mechanical characterization of geothermal reservoir rocks. *Paper presented at the European Geothermal Congress*.

Brace, W., & Byerlee, J. (1970). California earthquakes: Why only shallow focus? *Science*, *168*(3939), 1573–1575. https://doi.org/10.1126/science.168.3939.1573

Buijze, L., van Bijsterveldt, L., Cremer, H., Paap, B., Veldkamp, H., Wassing, B. B. T., et al. (2019). Review of induced seismicity in geothermal systems worldwide and implications for geothermal systems in the Netherlands. *Netherlands Journal of Geosciences*, *98*, e13. https://doi.org/10.1017/njg.2019.6

Byerlee, J. D. (1967). Frictional characteristics of granite under high confining pressure. *Journal of Geophysical Research*, *72*(14), 3639–3648. https://doi.org/10.1029/JZ072i014p03639

Byerlee, J. D. (1978). Friction of rocks. *Pure and Applied Geophysics*, *116*(4), 615–626. https://doi.org/10.1007/bf00876528

Cappa, F., Guglielmi, Y., Nussbaum, C., & Birkholzer, J. (2018). On the relationship between fault permeability increases, induced stress perturbation and the growth of aseismic slip during fluid injection. *Geophysical Research Letters*, *45*(20), 11012–011020. https://doi.org/10.1029/2018gl080233

Cappa, F., Scuderi, M. M., Collettini, C., Guglielmi, Y., & Avouac, J.-P. (2019). Stabilization of fault slip by fluid injection in the laboratory and in situ. *Science Advances*, *5*(3). eaau4065. https://doi.org/10.1126/sciadv.aau4065

Carter, N. L., & Kirby, S. H. (1978). Transient creep and semibrittle behavior of crystalline rocks. In *Rock friction and earthquake prediction* (pp. 807–839). Springer.

Catalli, F., Meier, M.-A., & Wiemer, S. (2013). The role of Coulomb stress changes for injection-induced seismicity: The Basel enhanced geothermal system. *Geophysical Research Letters*, *40*(1), 72–77. https://doi.org/10.1029/2012gl054147

Catalli, F., Rinaldi, A. P., Gischig, V., Nespoli, M., & Wiemer, S. (2016). The importance of earthquake interactions for injection-induced seismicity: Retrospective modeling of the Basel Enhanced Geothermal System. *Geophysical Research Letters*, *43*(10), 4992–4999. https://doi.org/10.1002/2016gl068932

Chang, K. W., & Segall, P. (2016). Injection-induced seismicity on basement faults including poroelastic stressing. *Journal of Geophysical Research: Solid Earth*, *121*(4), 2708–2726. https://doi.org/10.1002/2015jb012561

Deng, K., Liu, Y., & Harrington, R. M. (2016). Poroelastic stress triggering of the December 2013 Crooked Lake, Alberta, induced seismicity sequence. *Geophysical Research Letters*, *43*(16), 8482–8491. https://doi.org/10.1002/2016gl070421

De Simone, S., Carrera, J., & Vilarrasa, V. (2017). Superposition approach to understand triggering mechanisms of post-injection induced seismicity. *Geothermics*, *70*, 85–97. https://doi.org/10.1016/j.geothermics.2017.05.011

Ellsworth, W. L. (2013). Injection-Induced earthquakes. *Science*, *341*(6142), 1225942. https://doi.org/10.1126/science.1225942

Galis, M., Ampuero, J. P., Mai, P. M., & Cappa, F. (2017). Induced seismicity provides insight into why earthquake ruptures stop. *Science Advances*, *3*(12), eaap7528. https://doi.org/10.1126/sciadv.aap7528

Galis, M., Pelties, C., Kristek, J., Moczo, P., Ampuero, J. P., & Mai, P. M. (2015). On the initiation of sustained slip-weakening ruptures by localized stresses. *Geophysical Journal International*, *200*(2), 890–909. https://doi.org/10.1093/gji/ggu436

Grigoli, F., Cesca, S., Rinaldi, A. P., Manconi, A., López-Comino, J. A., Clinton, J. F., et al. (2018). The November 2017 Mw 5.5 Pohang earthquake: A possible case of induced seismicity in South Korea. *Science*, *360*(6392), 1003–0336. https://doi.org/10.1126/science.aat2010

Huang, K., Cheng, Q., Ghassemi, A., & Bauer, S. (2019). Investigation of shear slip in hot fractured rock. *International Journal of Rock Mechanics and Mining Sciences*, *120*, 68–81. https://doi.org/10.1016/j.ijrmms.2019.05.006

Im, K., & Avouac, J.-P. (2021). On the role of thermal stress and fluid pressure in triggering seismic and aseismic faulting at the Brawley Geothermal Field, California. *Geothermics*, *97*, 102238. https://doi.org/10.1016/j.geothermics.2021.102238

Im, K., Elsworth, D., Marone, C., & Leeman, J. (2017). The impact of frictional healing on stick-slip recurrence interval and stress drop: Implications for earthquake scaling. *Journal of Geophysical Research: Solid Earth*, *122*(12), 10102–110117. https://doi.org/10.1002/2017jb014476

Jeanne, P., Rutqvist, J., & Dobson, P. F. (2017). Influence of injection-induced cooling on deviatoric stress and shear reactivation of preexisting fractures in Enhanced Geothermal Systems. *Geothermics*, *70*, 367–375. https://doi.org/10.1016/j.geothermics.2017.08.003

Ji, Y., Fang, Z., & Wu, W. (2021). Fluid overpressurization of rock fractures: Experimental investigation and analytical modeling. *Rock Mechanics and Rock Engineering*, *54*(6), 3039–3050. https://doi.org/10.1007/s00603-021-02453-8

Ji, Y., Wanniarachchi, W. A. M., & Wu, W. (2020). Effect of fluid pressure heterogeneity on injection-induced fracture activation. *Computers and Geotechnics*, *123*, 103589. https://doi.org/10.1016/j.compgeo.2020.103589

Ji, Y., & Wu, W. (2020). Injection-driven fracture instability in granite: Mechanism and implications. *Tectonophysics*, *791*, 228572. https://doi.org/10.1016/j.tecto.2020.228572

Kim, K.-H., Ree, J.-H., Kim, Y., Kim, S., Kang, S. Y., & Seo, W. (2018). Assessing whether the 2017 Mw 5.4 Pohang earthquake in South Korea was an induced event. *Science*, *360*(6392), 1007–1009. https://doi.org/10.1126/science.aat6081

Kluge, C., Blöcher, G., Barnhoorn, A., & Bruhn, D. (2020). Hydraulic-mechanical properties of microfaults in granitic rock using the Punch-Through Shear test. *International Journal of Rock Mechanics and Mining Sciences*, *134*, 104393. https://doi.org/10.1016/j.ijrmms.2020.104393

Ladner, F., & Häring, M. O. (2009). Hydraulic characteristics of the basel 1 enhanced geothermal system. *GRC Transactions*, *33*, 199–203.

Marone, C. (1998). The effect of loading rate on static friction and the rate of fault healing during the earthquake cycle. *Nature*, *391*(6662), 69–72. https://doi.org/10.1038/34157

Marone, C., Vidale, J. E., & Ellsworth, W. L. (1995). Fault healing inferred from time dependent variations in source properties of repeating earthquakes. *Geophysical Research Letters*, *22*(22), 3095–3098. https://doi.org/10.1029/95GL03076

McGarr, A. (2014). Maximum magnitude earthquakes induced by fluid injection. *Journal of Geophysical Research: Solid Earth*, *119*(2), 1008–1019. https://doi.org/10.1002/2013jb010597

McLaskey, G. C., Thomas, A. M., Glaser, S. D., & Nadeau, R. M. (2012). Fault healing promotes high-frequency earthquakes in laboratory experiments and on natural faults. *Nature*, *491*(7422), 101–104. https://doi.org/10.1038/nature11512

McLaskey, G. C., & Yamashita, F. (2017). Slow and fast ruptures on a laboratory fault controlled by loading characteristics. *Journal of Geophysical Research: Solid Earth*, *122*(5), 3719–3738. https://doi.org/10.1002/2016jb013681

Mukuhira, Y., Dinske, C., Asanuma, H., Ito, T., & Häring, M. O. (2016). Pore pressure behavior at the shut-in phase and causality of large induced seismicity at Basel, Switzerland. *Journal of Geophysical Research: Solid Earth*, *122*(1), 411–435. https://doi.org/10.1002/2016jb013338

Noël, C., Passelègue, F. X., Giorgetti, C., & Violay, M. (2019). Fault reactivation during fluid pressure oscillations: Transition from stable to unstable slip. *Journal of Geophysical Research: Solid Earth*, *124*(11), 10940–10953. https://doi.org/10.1029/2019jb018517

Ohnaka, M., & Shen, L.-f. (1999). Scaling of the shear rupture process from nucleation to dynamic propagation: Implications of geometric irregularity of the rupturing surfaces. *Journal of Geophysical Research: Solid Earth*, *104*(B1), 817–844. https://doi.org/10.1029/1998jb900007

Olasolo, P., Juárez, M. C., Morales, M. P., D´Amico, S., & Liarte, I. A. (2016). Enhanced geothermal systems (EGS): A review. *Renewable and Sustainable Energy Reviews*, *56*, 133–144. https://doi.org/10.1016/j.rser.2015.11.031

Olsen, M. P., Scholz, C. H., & Léger, A. (1998). Healing and sealing of a simulated fault gouge under hydrothermal conditions: Implications for fault healing. *Journal of Geophysical Research: Solid Earth*, *103*(B4), 7421–7430. https://doi.org/10.1029/97JB03402

Passelègue, F. X., Aubry, J., Nicolas, A., Fondriest, M., Deldicque, D., Schubnel, A., & Di Toro, G. (2019). From fault creep to slow and fast earthquakes in carbonates. *Geology*, *47*(8), 744–748. https://doi.org/10.1130/g45868.1

Passelegue, F. X., Brantut, N., & Mitchell, T. M. (2018). Fault reactivation by fluid injection: Controls from stress state and injection rate. *Geophysical Research Letters*, *45*(23), 12837–812846. https://doi.org/10.1029/2018GL080470

Reches, Z., & Lockner, D. A. (2010). Fault weakening and earthquake instability by powder lubrication. *Nature*, *467*(7314), 452–455. https://doi.org/10.1038/nature09348

Rutter, E., & Hackston, A. (2017). On the effective stress law for rock-on-rock frictional sliding, and fault slip triggered by means of fluid injection. *Philosophical Transactions of the Royal Society A: Mathematical, Physical & Engineering Sciences*, *375*(2103), 20160001. https://doi.org/10.1098/rsta.2016.0001

Rutter, E. H., & Maddock, R. H. (1992). On the mechanical properties of synthetic kaolinite/quartz fault gouge. *Terra Nova*, *4*(4), 489–500. https://doi.org/10.1111/j.1365-3121.1992.tb00585.x

Rutter, E. H., & Mainprice, D. H. (1978). The effect of water on stress relaxation of faulted and unfaulted sandstone. *Pure and Applied Geophysics PAGEOPH*, *116*(4–5), 634–654. https://doi.org/10.1007/bf00876530

Schoenball, M., Ajo-Franklin, J. B., Blankenship, D., Chai, C., Chakravarty, A., Dobson, P., et al. (2020). Creation of a mixed-mode fracture network at mesoscale through hydraulic fracturing and shear stimulation. *Journal of Geophysical Research: Solid Earth*, *125*(12), e2020JB019807. https://doi.org/10.1029/2020jb019807

Schoenball, M., & Ellsworth, W. L. (2017). A systematic assessment of the spatiotemporal evolution of fault activation through induced seismicity in Oklahoma and Southern Kansas. *Journal of Geophysical Research: Solid Earth*, *122*(12), 10189–110206. https://doi.org/10.1002/2017jb014850

Scholz, C. H. (1998). Earthquakes and friction laws. *Nature*, *391*(6662), 37–42. https://doi.org/10.1038/34097

Segall, P., & Lu, S. (2015). Injection-induced seismicity: Poroelastic and earthquake nucleation effects. *Journal of Geophysical Research: Solid Earth*, *120*(7), 5082–5103. https://doi.org/10.1002/2015jb012060

Stesky, R. M., Brace, W. F., Riley, D. K., & Robin, P. Y. F. (1974). Friction in faulted rock at high temperature and pressure. *Tectonophysics*, *23*(1), 177–203. https://doi.org/10.1016/0040-1951(74)90119-X

Tembe, S., Lockner, D. A., & Wong, T.-F. (2010). Effect of clay content and mineralogy on frictional sliding behavior of simulated gouges: Binary and ternary mixtures of quartz, illite, and montmorillonite. *Journal of Geophysical Research*, *115*(B3), B03416. https://doi.org/10.1029/2009jb006383

Tenthorey, E., Cox, S. F., & Todd, H. F. (2003). Evolution of strength recovery and permeability during fluid–rock reaction in experimental fault zones. *Earth and Planetary Science Letters*, *206*(1–2), 161–172. https://doi.org/10.1016/S0012-821X(02)01082-8

Wang, L., Kwiatek, G., Rybacki, E., Bonnelye, A., Bohnhoff, M., & Dresen, G. (2020). Laboratory study on fluid-induced fault slip behavior: The role of fluid pressurization rate. *Geophysical Research Letters*, *47*(6), e2019GL086627. https://doi.org/10.1029/2019gl086627

Xu, S., Fukuyama, E., Yamashita, F., Mizoguchi, K., Takizawa, S., & Kawakata, H. (2018). Strain rate effect on fault slip and rupture evolution: Insight from meter-scale rock friction experiments. *Tectonophysics*, *733*, 209–231. https://doi.org/10.1016/j.tecto.2017.11.039

Yasuhara, H., Marone, C., & Elsworth, D. (2005). Fault zone restrengthening and frictional healing: The role of pressure solution. *Journal of Geophysical Research*, *110*(B6), B06310. https://doi.org/10.1029/2004jb003327

References From the Supporting Information

Almakari, M., Chauris, H., Passelègue, F., Dublanchet, P., & Gesret, A. (2020). Fault's hydraulic diffusivity enhancement during injection induced fault reactivation: Application of pore pressure diffusion inversions to laboratory injection experiments. *Geophysical Journal International*, *223*(3), 2117–2132. https://doi.org/10.1093/gji/ggaa446

Ji, Y., Kluge, C., Hofmann, H., & Blöcher, G. (2022). Effects of external temperature and dead volume on laboratory measurements of pore pressure and injected volume in a rock fracture. *Journal of Rock Mechanics and Geotechnical Engineering*, *4*(5), 1461–1469. https://doi.org/10.1016/j.jrmge.2021.12.007

Pei, L., Blöcher, G., Milsch, H., Zimmermann, G., Sass, I., & Huenges, E. (2017). Thermo-mechanical properties of Upper Jurassic (Malm) carbonate rock under drained conditions. *Rock Mechanics and Rock Engineering*, *51*(1), 23–45. https://doi.org/10.1007/s00603-017-1313-0

Shapiro, S. A., Huenges, E., & Borm, G. (1997). Estimating the crust permeability from fluid-injection-induced seismic emission at the KTB site. *Geophysical Journal International*, *131*(2), F15–F18. https://doi.org/10.1111/j.1365-246X.1997.tb01215.x